Aerosol Science and Technology

ISSN: 0278-6826 (Print) 1521-7388 (Online) Journal homepage: https://www.tandfonline.com/loi/uast20

Numerical Investigation of Sheath and Aerosol Flows in the Flow Combination Section of a Baron Fiber Classifier

Prahit Dubey, Urmila Ghia & Leonid A. Turkevich

To cite this article: Prahit Dubey, Urmila Ghia & Leonid A. Turkevich (2014) Numerical Investigation of Sheath and Aerosol Flows in the Flow Combination Section of a Baron Fiber Classifier, Aerosol Science and Technology, 48:8, 896-905, DOI: 10.1080/02786826.2014.936342

To link to this article: https://doi.org/10.1080/02786826.2014.936342

Aerosol Science and Technology, 48:896–905, 2014
Published with license by Taylor & Francis
ISSN: 0278-6826 print / 1521-7388 online
DOI: 10.1080/02786826.2014.936342

Numerical Investigation of Sheath and Aerosol Flows in the Flow Combination Section of a Baron Fiber Classifier

Prahit Dubey,[1] Urmila Ghia,[1] and Leonid A. Turkevich[2]
[1]*Department of Mechanical and Materials Engineering, College of Engineering and Applied Science, University of Cincinnati, Cincinnati, Ohio, USA*
[2]*Chemical Exposure and Monitoring Branch, Division of Applied Research and Technology, National Institute for Occupational Safety and Health, Centers for Disease Control and Prevention, Cincinnati, Ohio, USA*

The Baron fiber classifier is an instrument used to separate fibers by length. The flow combination section (FCS) of this instrument is an upstream annular region, where an aerosol of uncharged fibers is introduced along with two sheath flows; length separation occurs by dielectrophoresis downstream in the flow classification section. In its current implementation at NIOSH, the instrument is capable of processing only very small quantities of fibers. In order to prepare large quantities of length-separated fibers for toxicological studies, the throughput of the instrument needs to be increased, and hence, higher aerosol flow rates need to be considered. However, higher aerosol flow rates may give rise to flow separation or vortex formation in the FCS, arising from the sudden expansion of the aerosol at the inlet nozzle. The goal of the present investigation is to understand the interaction of the sheath and aerosol flows inside the FCS, using computational fluid dynamics (CFD), and to identify possible limits to increasing aerosol flow rates. Numerical solutions are obtained using an axisymmetric model of the FCS, and solving the Navier–Stokes equations governing these flows; in this study, the aerosol flow is treated purely aerodynamically. Results of computations are presented for four different flow rates. The geometry of the converging outer cylinder, along with the two sheath flows, is effective in preventing vortex formation in the FCS for aerosol-to-sheath flow inlet velocity ratios below ∼50. For higher aerosol flow rates, recirculation is observed in both inner and outer sheaths. Results for velocity, streamlines, and shear stress are presented.

1. INTRODUCTION

Exposure to airborne fibers, such as asbestos, is known to cause lung cancer, mesothelioma, and other pleural disorders in humans (NIOSH 2011). There is a long experimental history associating fiber length with cytotoxicity. In an epidemiological study, Lippmann (1990) correlated fiber length with asbestosis, mesothelioma, and lung cancer. Hart et al. (1994) exposed hamster ovary cells to several inorganic fibers (e.g., glass, asbestos) and found fiber length to be correlated with toxicity. In an in vitro study, Blake et al. (1998) used a rat alveolar macrophage microculture to show that longer glass fibers are more toxic than shorter fibers. Recent epidemiological studies (Stayner et al. 2008; Loomis et al. 2010) indicated a higher risk of lung cancer with exposure to fibers longer than 10 μm. A direct experimental evaluation of the role of fiber length in cytotoxicity requires a sufficient sample of length-separated fibers (NIOSH 2011).

The Baron fiber classifier utilizes dielectrophoresis to separate fibers by length (Baron et al. 1994; Han et al. 1994; Deye et al. 1999; Wang et al. 2005). This classifier has been used by NIOSH to prepare samples for in vitro testing of the role of length in fiber toxicity (Ye et al. 1999; Castranova et al. 1996, 2000, 2003; Zeidler et al. 2001; Zeidler-Erdely et al. 2006). NIOSH is currently increasing the throughput of this Baron classifier to produce quantities of length-selected fibers sufficient for toxicological investigation (Turkevich and Deye, 2011).

The Baron fiber classifier (Baron 1993; Baron et al. 2001, 2002) consists (Figure 1a) of two major sections, namely, a flow combination section (FCS) and, downstream, a flow classification section.

The flow classification section consists of two concentric metal cylinders across which a large electric field is imposed. An aerosol of uncharged fibers is introduced into the annular gap between the cylinders, and the fibers experience both an aerodynamic drag and the force due to the imposed electric field. The curved geometry concentrates the electric field on the inner cylinder. The electric field polarizes the neutral fibers, which align parallel to the electric field (Lilienfeld

Received 6 September 2013; accepted 1 April 2014.
Address correspondence to Leonid A. Turkevich, Chemical Exposure and Monitoring Branch, Division of Applied Research and Technology, National Institute for Occupational Safety and Health, Centers for Disease Control and Prevention, 4676 Columbia Parkway, Cincinnati, OH 45226, USA. E-mail: LLT0@cdc.gov

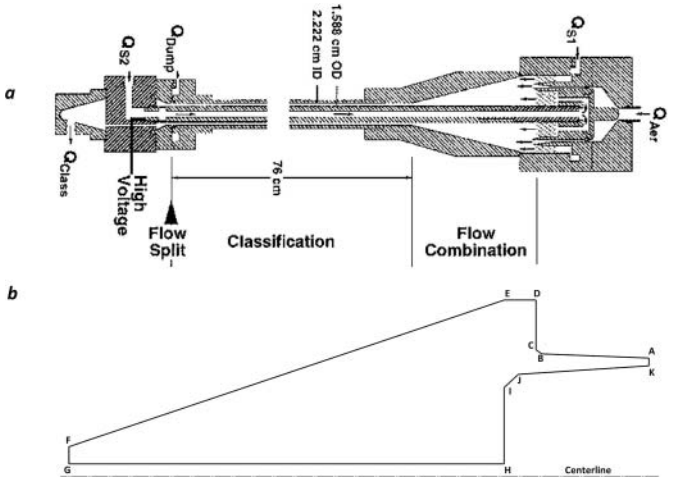

FIG. 1. Schematic representation of (a) Baron fiber classifier (Deye et al. 1999), and (b) flow combination section; dimensionless lengths listed in Table S1.

1985) and migrate toward the inner cylinder. Longer fibers experience a larger polarization (Lipowicz and Yeh 1989), and these are deposited upstream on the inner cylinder (electrode). The shorter fibers experience a smaller polarization, and hence, a smaller electric force of attraction to the inner cylinder; these either deposit downstream on the inner cylinder, or are removed at the bottom of classifier (Deye et al. 1999).

Upstream of the flow classification section is the FCS, which consists (Figure 1b) of the same inner cylinder (HG) as in the flow classification section, and a converging outer cylinder (EF). The fiber-containing aerosol is introduced via an annular nozzle (AK) and is then sandwiched between two annular sheath flows (introduced through open-pore-foam flow straighteners IH and CD). The outer cylinder converges as a cone EF over the length of the FCS. The FCS is designed to produce a nearly "parabolic" flow profile at the entrance FG to the flow classification region of the instrument.

The use of sheath flows is not uncommon in aerosol instruments and is well known (Knutson and Whitby 1975) in its use in the differential mobility analyzer (DMA). The classical DMA consists of an annular region between two concentric cylinders–similar to the flow classification section of the Baron instrument, but with only a single sheath stream adjacent to the inner cylinder. The resolution of the DMA, in the non-diffusive regime, scales as $R \sim \beta^{-1}$, where $\beta \sim Q_{\text{aero}}/Q_{\text{sh}}$, where Q_{aero} and Q_{sh} are, respectively, the aerosol and sheath volumetric flow rates (Flagan 1998, 1999, 2001). The results of the present study should have applicability to the design and operation of this class of aerosol instruments, especially in situations where higher aerosol flows are contemplated.

While the Baron instrument (in its current configuration) is effective in separating fibers on the basis of their length, it is capable of processing only very small quantities of fibers. In order to increase the throughput of the Baron classifier, so as to produce quantities of length-separated fibers sufficient for toxicological studies, the aerosol flow rate needs to be increased, and this motivates a critical analysis of higher aerosol flows within the Baron classifier. In particular, the FCS is susceptible to flow separation and vortex formation owing to the sudden expansion of the aerosol at the nozzle exit and the relatively high ratio of the aerosol velocity to the sheath velocities. This study models the higher flows in this section of the Baron instrument.

Deye et al. (1999) conducted a detailed testing of the performance of the Baron classifier. To accompany their experimental diagnostics, they calculated approximate particle trajectories within the flow classification section; they also provided a computational fluid dynamics (CFD) study of the FCS. They concluded that the Baron classifier falls short of its theoretical efficiency. They provided streamlines and velocity contours but did not provide a detailed analysis of the velocity, pressure, and shear stress profiles within the FCS. Their CFD analysis was performed only for the currently utilized flow rates. The goal of the present study is to conduct a more extended, yet still purely aerodynamic (i.e., single phase) CFD analysis of the aerosol and sheath flows in order to explore flow rate limitations of the Baron instrument.

The present CFD work considered an axisymmetric model of the FCS (a three-dimensional simulation is discussed in the online supplemental information [SI]), and examined velocity, pressure, and shear stress for four different sets of flow rates (Table S5 in the SI). The choice of flow rates permitted the probing of possible flow separation or vortex formation that might develop. Case 1 embodies the flow rates used by NIOSH in the classifier's current implementation. For Case 2, only the aerosol flow rate is increased by a factor of 10, leaving the sheath flows at their original levels. The results of this simulation provided insight into the effectiveness of the sheath flows in keeping an increased aerosol flow away from the FCS walls. The aerosol flow rate was further increased by a factor of 15 and 20 in Cases 3 and 4, respectively. For these cases, toroidal vortices develop, due to the large shear between the aerosol and sheath flows. In all of our simulations, the flow is laminar.

2. METHOD

2.1. Geometry

The FCS (Figure 1b) is bounded by two concentric cylinders; the outer cylinder radius reduces from $r_{\text{E}} = r_{\text{D}} = 3.81$ cm to $r_{\text{F}} = 1.11$ cm over the axial length HG, causing a conical constriction of the flow, before the combined flow enters the flow classification section of the instrument. The nozzle is radially asymmetrical in shape, flaring toward the outer cylinder, with the outer edge terminating at BC and the longer inner edge extending to IJ. The radial location of this annular nozzle is closer to the outer cylinder than to the inner cylinder. Dimensionless radii, r^*, and axial lengths, x^*, are scaled to the initial outer cylinder radius $r_{\text{E}} = r_{\text{D}} = 3.81$ cm

(Table S1). Dimensionless velocities, v^*, are scaled to the initial outer sheath velocity, $v_{\text{out sh}} = 3.89$ cm/s. The pressure and axial shear stress, $\sigma_{xr} = -\mu\left(\frac{\partial v_r}{\partial x} + \frac{\partial v_x}{\partial r}\right)$, are made dimensionless by reference to $^1/_2\, \rho\, v_{\text{out sh}}{}^2$.

2.2. Grid Generation

Grid generation is an important part of any CFD simulation. The grid has a significant impact on the rate of convergence, on solution accuracy and on the CPU time required for the solution. An appropriate grid needs to resolve the inlet region of the entering annular flows and the regions near the wall. Pointwise 16.02 was used to generate a high-quality structured multi-block mesh for the complex FCS geometry, which has several high-gradient regions. Details are discussed in the SI (Tables S2 and S3; Celik et al. 2008).

2.3. Mathematical Formulation

The governing equations for the present flow are the continuity and the Navier–Stokes equations. The flow is treated as incompressible and is laminar (Reynolds number Re < 2000): for Case 1, at the aerosol nozzle entrance, $\text{Re}_{\text{AK}} \approx 14$; at the outer sheath inlet, $\text{Re}_{\text{CD}} \approx 25$; at the inner sheath inlet, $\text{Re}_{\text{HI}} \approx 50$; at the FCS exit, $\text{Re}_{\text{FG}} \approx 400$.

For an incompressible fluid, the continuity equation reduces to

$$\nabla . \vec{v} = 0 \qquad [1]$$

and the momentum equation becomes

$$\frac{\partial(\rho \vec{v})}{\partial t} + \nabla . \left(\rho \vec{v} \vec{v}\right) = -\nabla p + \nabla . (\bar{\bar{\tau}}) \qquad [2]$$

where the stress tensor is

$$\bar{\bar{\tau}} = \mu \left[\left(\nabla \vec{v} + \nabla \vec{v}^T \right) - \frac{2}{3} \nabla . \vec{v} \bar{\bar{I}} \right], \qquad [3]$$

and $\vec{v}$ is the velocity field, p is the static pressure, ρ and μ are, respectively, the density and the dynamic viscosity of air, and $\bar{\bar{I}}$ is the identity tensor. Gravity has negligible impact on the air flow, so there is no body-force term in Equation (2).

2.4. Numerical Solution

The equations were solved numerically using a finite-volume solver (Fluent 6.3, based on an algorithm of Patankar 1980). A pressure-based solver (incompressible flow) is used, with SIMPLE (semi-implicit method for pressure-linked equations) as the pressure–velocity coupling method, with the default values for the relaxation parameters (0.3 for continuity and 0.7 for momentum)–we note that convergence was fastest when these relaxation parameters were used. A second-order up-winding scheme for convective terms, and a second-order central-differenced scheme for diffusion terms were used to integrate the equations in space (our results do not appear to change when a third-order upstream centered scheme, MUSCL, is used instead for the convection terms). Temporal discretization was performed using a second-order implicit scheme.

2.5. Material Selection

In our calculations, all three fluids (aerosol, inner, and outer sheaths) are taken to be dry air at $T = 20°\text{C}$ (The fiber concentration in the NIOSH instrument is $n_{\text{aero}} \sim 6 \times 10^4$ fibers/cm^3, which corresponds to a solids volume fraction of $\phi \sim 6 \times 10^{-7}$; this low solid volume fraction motivates a purely aerodynamic treatment of the aerosol flow.). In the operation of the Baron classifier, both the aerosol and sheath flow air need to be humidified to RH = 50%, so as to facilitate fiber polarization (Wang et al. 2005), as well as to minimize Coulombic fiber–fiber interactions (Turkevich and Deye, 2011). However, for our simulations, we have neglected humidity; while humidity influences the fiber polarization, it is not expected to alter the aerodynamics of the aerosol.

2.6. Boundary Conditions

The aerosol is introduced at the nozzle inlet (AK) with a uniform inlet velocity. The nozzle axial length AB = 3.17 cm is 25 times longer than its hydraulic diameter at the inlet: the entrance length (calculated for a straight annulus, using the hydraulic diameter), for the Case 1 flow rates, is 0.085 cm. The uniform inlet velocity profile (at AK) will thus become fully developed flow by the nozzle exit (BJ). The sheath flows are introduced via foam diffusers (at CD and HI) so that these flows enter the FCS with uniform inlet velocity. The nozzle and FCS surfaces are non-porous solid walls, with zero tangential (no-slip) and normal components of the velocities at the walls. The outlet pressure (at FG) is set at gauge pressure ($p = 0$).

2.7. Convergence Criterion

The solution of the equations was considered to be converged when the scaled residuals for the continuity and momentum equations decreased to 10^{-12} (from initial values $\sim 10^{-1}$). All simulations were performed under this convergence criterion.

2.8. Streamlines

In cylindrical coordinates, the axial velocity, v_x, is related to the stream function, ψ, by

$$v_x = \frac{1}{r} \frac{\partial \psi}{\partial r}, \qquad [4]$$

which is easily integrated at the inlet, as the inlet axial velocity is uniform. If ψ_1 and ψ_2 represent values of the stream function at radial locations r_1 and r_2 at the inlet, then

$$\Delta\psi = \psi_2 - \psi_1 = v_x \frac{r_2^2 - r_1^2}{2}. \quad [5]$$

This permits an identification of streamline contour values (Figure S3, where we have used uniform contour spacing, given in Table S7).

3. RESULTS AND DISCUSSION

In this section, we present and discuss the results of our CFD simulations. Special attention is given to the flow velocities, pressure, and shear stress. We also compare our results (Case 1) with those obtained previously (Deye et al. 1999).

3.1. Axial Velocity and Shear Stress Profiles

3.1.1. Importance of the Sheath Flows

In order to understand the effect of sheath flows, we considered a preliminary case, in which the sheath flows have been suppressed, while the aerosol flow rate is kept the same as in Case 1. This is discussed in detail in the SI. Even though the flow remains steady and laminar (Re < 20), toroidal vortices develop on either side of the nozzle (near the outer and inner cylinders). The aerosol jet quickly expands to the confining cylinders; aerosol deposition on the cylinder walls may be expected immediately downstream from the vortices. As will be seen below, a major effect of the sheath flows is to suppress vortex formation within the FCS.

3.1.2. Case 1

The flow rates for Case 1 are the flow rates used in the current implementation of the NIOSH instrument (Deye et al. 1999). The aerosol flow rate is 1 L/min, while the sheath flow rates are each 4.5 L/min: $v_{aero}/v_{in\ sh} = 3.96$, $v_{aero}/v_{out\ sh} = 3.12$.

The development of the non-dimensional axial velocity, u^*, as a function of the non-dimensional axial distance, x^*, is shown in Figure 2. The nozzle outer edge terminates at $x^* = 0.860$ (before the inner edge), where the aerosol enters the FCS; the outer sheath is also introduced into the FCS as plug flow at $x^* = 0.860$. The zero slip on the nozzle outer edge gives rise to the local minimum at $x^* = 0.900$, $r^* \sim 0.75$; as the outer sheath and aerosol flow develop, this local minimum eventually disappears by $x^* = 1.013$. The inner sheath flow is introduced as plug flow at $x^* = 1.013$, and contacts the combined outer sheath and aerosol flow. The zero slip on the nozzle inner edge results in a local minimum at $x^* = 1.100$, $r^* \sim 0.660$, as the aerosol contacts the inner sheath flow. The velocity of the flow is higher close to the inner wall, a direct result of the introduced inner sheath velocity. As the outer wall of the FCS converges along the length, reducing the cross-sectional area, the average axial velocity increases (so as to conserve mass flow). At the FCS exit ($x^* = 4.347$), the radial profile of the axial velocity is very nearly parabolic. Note the different velocity scales used in these figures.

The radial variation of the axial velocity is primarily responsible for the behavior of the shear stress (Figure 3); the higher gradient of axial velocity results in a higher shear stress. The local minimum ($x^* = 1.100$) of the axial velocity, and concomitant local maximum of the shear stress gradually decrease ($x^* = 1.500$), and finally disappear ($x^* = 2.000$), with the development of the axial velocity profile. The large shear stress near each of the cylinder walls is a direct result of the high velocity gradient near the walls. At the exit ($x^* = 4.347$), the shear stress is radially sigmoidal (with higher shear stress near the walls, and zero shear stress near the center of the annulus).

We have performed an additional simulation (not discussed in this report), where all three of the flow rates have been

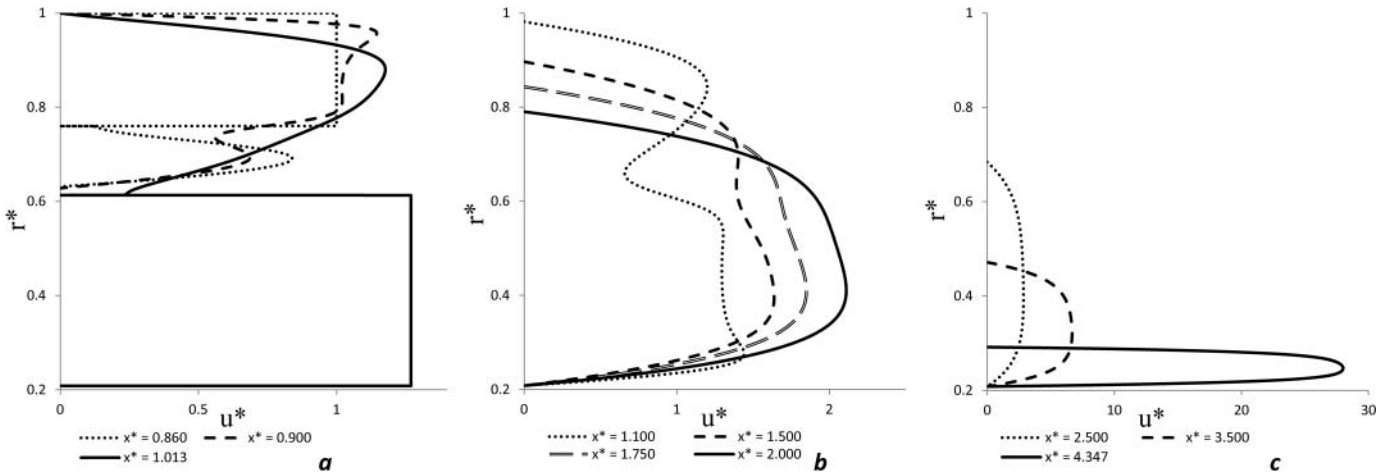

FIG. 2. Non-dimensional axial velocity profiles for Case 1.

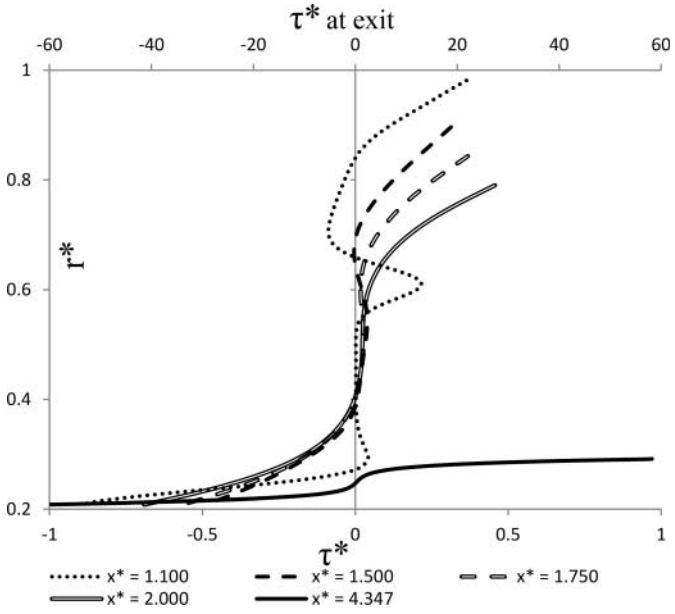

FIG. 3. Radial distribution of shear stress for Case 1.

increased by a factor of 4. The total flow rate at the exit becomes $Q_{tot} = 40$ L/min, so that the local Reynolds number at the exit Re $\sim$ 1524, just below the transition ($Re_c \sim 2000$) to turbulent flow in the annular duct (Hanks and Bonner 1971; Dou et al. 2010). Qualitatively, all the flow characteristics of Case 1 are retained.

3.1.3. Case 2

In this case, the aerosol flow rate was increased to 10 L/min (by a factor of 10 from Case 1), while the sheath flow rates were kept at 4.5 L/min: $v_{aero}/v_{in\ sh} = 39.57$, $v_{aero}/v_{out\ sh} = 31.17$. Detailed descriptions of the flow profile and shear stress are contained in the SI. Qualitatively, the "finger" velocity profile of the aerosol is present from the initial injection, the slower sheaths merging into the aerosol as the flow progresses downstream, evolving into a roughly parabolic exit profile. Oscillations in the shear stress are more pronounced than in Case 1, but the desired sigmoidal stress profile is still recovered at the exit.

3.1.4. Case 3

In this case, the aerosol flow rate was further increased to 15 L/min, while keeping each sheath flow at 4.5 L/min: $v_{aero}/v_{in\ sh} = 59.35$, $v_{aero}/v_{out\ sh} = 46.76$.

The non-dimensional axial velocity profiles, u^*, as a function of non-dimensional axial distance, x^*, are shown in Figure 4. The velocity protrusion (at $r^* \sim 0.7$ for the $x^* = 0.900$ profile) is larger in magnitude than in Case 2, owing to the higher aerosol flow rate. The zero slip at the nozzle upper edge gives rise to a local minimum ($r^* \sim 0.760$). Notice that the change in velocity scale causes this local minimum to appear fairly flat. Downstream ($x^* = 1.013$), this local minimum washes out; however, the velocity protrusion is reduced only slightly. At $x^* = 1.100$, unlike in Case 2, the higher aerosol velocity stretches the tip out so that the local minimum (at $r^* \sim 0.620$ in Case 2) is less prominent. Momentum is transferred from the aerosol to the sheath flows during the downstream progression of the flow, and the velocity minimum gradually disappears. However, the tip of the nozzle remains prominent, because of the high aerosol velocity, and it takes the flow a longer distance to develop ($x^* = 1.750$). At $x^* = 1.750$, the velocity is negative for $0.80 < r^* < 0.85$; this is a signature of a recirculation region, confirmed by an analysis of the streamlines (discussed below). The small negative value of the velocity indicates the weakness of this vortex. Again, at the exit ($x^* = 4.347$), the velocity profile is radially quite parabolic.

Radial variations of shear stress at various axial distances, x^*, are shown in Figure 5. The effect of the recirculation on the shear stress is apparent at $x^* = 1.750$, where the shear

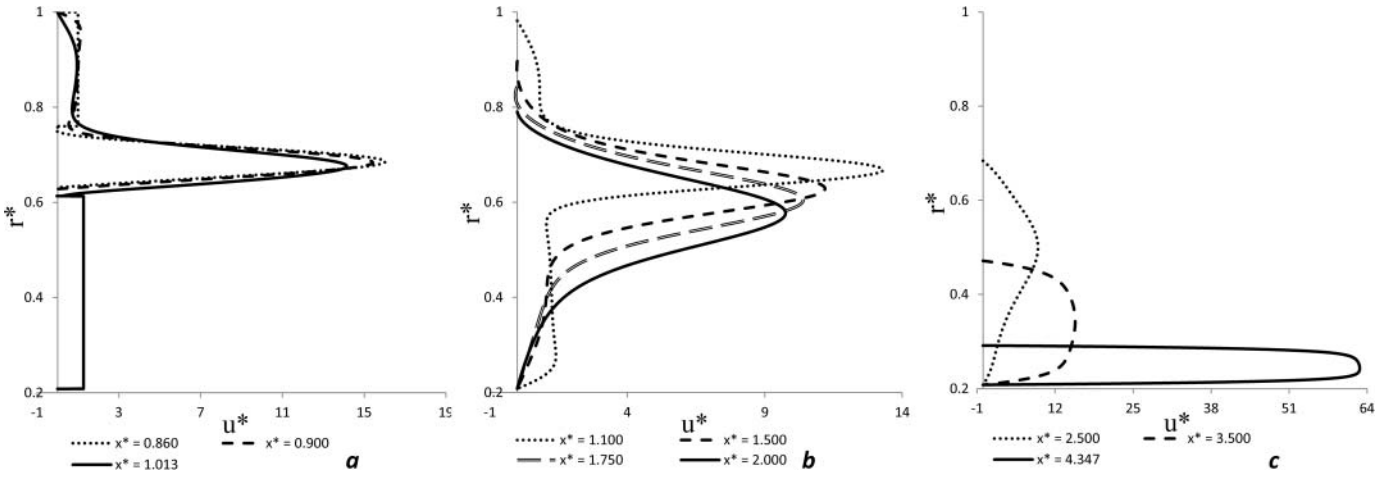

FIG. 4. Non-dimensional axial velocity profiles for Case 3.

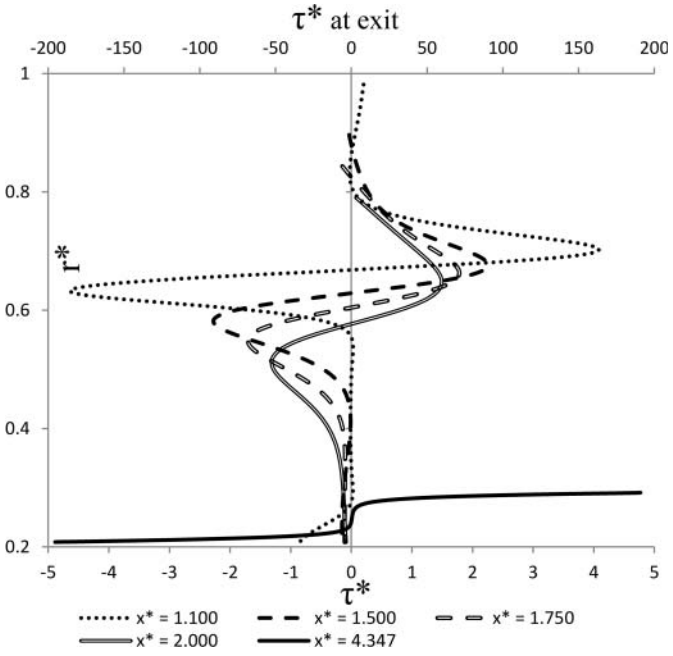

FIG. 5. Radial distribution of shear stress for Case 3.

stress becomes negative. At the exit, the shear stress remains radially sigmoidal, with no evidence of the upstream recirculation.

3.1.5. *Case 4*

In this case, the aerosol flow rate was increased to 20 L/min, while keeping each sheath flow at 4.5 L/min: $v_{aero}/v_{in\ sh} = 79.14$, $v_{aero}/v_{out\ sh} = 62.35$. Detailed descriptions of the velocity and shear stress profiles are contained in the supplemental material. Compared with Case 3, a second recirculation now forms near the inner cylinder. Despite the presence of both weak recirculation regions, the qualitative behavior of both the velocity and the shear stress profiles are very similar to those of Case 3, with the desired parabolic flow profile and the desired sigmoidal shear stress profile being achieved at the exit of the FCS.

3.1.6. *Summary*

In summary, the radial profiles of the axial velocity and shear stress for Case 1 (current flows of the Baron instrument) exhibit the desired laminar, focused aerosol behavior, free from any recirculation; this flow behavior is maintained even when all of the flows are increased evenly by a factor of 4. Increasing the aerosol flow rate by a factor of 10, without increasing the sheath flow rates (Case 2), maintains this flow behavior. When the aerosol flow rate is increased by a factor of 15 (Case 3), a vortex develops near the outer cylinder; when the aerosol flow rate is increased by a factor of 20 (Case 4), a second vortex develops near the inner cylinder. This behavior will be clarified with a streamline analysis. However, in all the cases studied, despite the detailed flow variations within the FCS itself, the instrument design is sufficiently robust so that the aerosol velocity exhibits the desired parabolic flow profile, with the concomitant desired sigmoidal shear stress profile, upon exiting the FCS.

3.2. Streamlines

All of the flows studied are steady and laminar; the aerosol streamlines are preserved, and the aerosol never mixes with the sheath flows. For a typical fiber ($d \sim 1\ \mu$m, $L \sim 10\ \mu$m, which yields an aerodynamic diameter $d_{aero} \sim 1\ \mu$m), we can calculate a Stokes number, $\mathrm{Stk} = (\rho_{part}/\rho_{air})^*(d_{part}{}^2\ U)/(18\ \nu_{air}\ D)$, where we consider glass fibers ($\rho_{part} \sim 2.58$ g/cm^3), and where we take the nozzle width as the sharpest length scale over which the flow can be diverted, $D \sim r_A - r_K = 0.64$ cm. For Case 1 (the usual operation of the Baron instrument), the aerosol velocity at the nozzle is $U \sim 15.4$ cm/s, whence $\mathrm{Stk} \sim 2 \times 10^{-4}$; for Case 4 (the most extreme case considered), $\mathrm{Stk} \sim 4 \times 10^{-3}$. These estimates hardly change when asbestos is used instead of glass. Figure 6 shows the streamline contours (uniform contour spacing, given in Table S7) for the different cases studied.

The streamlines for Case 1 ($Q_{aero}/Q_{sheath} = 0.22$, $v_{aero}/v_{in\ sh} = 3.96$, $v_{aero}/v_{out\ sh} = 3.12$) are shown in Figure 6a. The flow is free from recirculation. The fibers are confined near the middle region at the exit, away from the walls. The presence of the sheath flows (Figure 6a) inhibits the formation of recirculation regions (toroidal vortices), which develop in the entrance region near the outer and inner cylinders when these sheath flows are absent (Figure S3). Also, in the absence of sheath flows, the aerosol, emerging from the nozzle, tends to spread out along with the edges (at the exit, the aerosol extends over the entire annular region $0.210 < r^* < 0.291$). The sheath

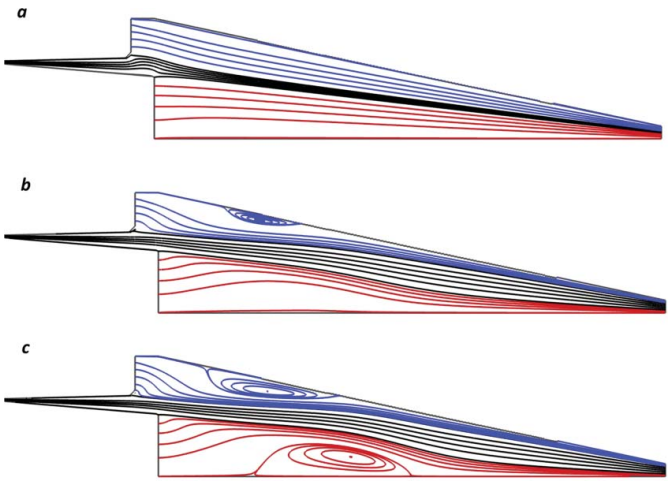

FIG. 6. Streamlines for: (a) Case 1, (b) Case 3, (c) Case 4; black represents aerosol, blue, and red represent outer and inner sheath flow, respectively.

layer is effective in confining the aerosol, preventing deposition on the walls (at the exit, the aerosol is confined to the central annular region $0.249 < r^* < 0.255$). The bending of the streamlines near the nozzle edges is strongly affected by the sheath flows: without the protection of the outer sheath flow, the aerosol would deposit on the outer wall (as suggested by Figure S3) as it emerges from the upper end of the nozzle; the sheath flows (Figure 6a) refocus the aerosol annulus and inhibit wall deposition.

In Case 2 (no illustration), the aerosol flow rate has been increased 10-fold ($Q_{aero}/Q_{sheath} = 2.22$, $v_{aero}/v_{in\ sh} = 39.57$, $v_{aero}/v_{out\ sh} = 31.17$) without vortex formation; at this higher aerosol flow, at the exit, the aerosol now extends over a slightly expanded annular region $0.233 < r^* < 0.271$.

Case 3, which represents a further increase (15-fold) in the aerosol flow rate ($Q_{aero}/Q_{sheath} = 3.33$, $v_{aero}/v_{in\ sh} = 59.35$, $v_{aero}/v_{out\ sh} = 46.76$), suggests a possible flow rate limitation of the FCS. Figure 6b shows the streamlines at $t = 5$ s following the flow initiation (steady state has been achieved at this time). A weak recirculation region has developed near the outer wall. The origin of this recirculation may be tracked with earlier time solutions ($t = 0.1$, 0.2, 0.3 s, computed with convergence at each time step). At the earlier times, the velocity mismatch, between the aerosol and the outer sheath flow, initiates the formation of a vortex near the entrance region, which is then pushed downstream, close to the outer cylinder.

Figure 6c shows the streamlines for Case 4. At this further (20-fold) increase in the aerosol flow rate ($Q_{aero}/Q_{sheath} = 4.44$, $v_{aero}/v_{in\ sh} = 79.14$, $v_{aero}/v_{out\ sh} = 62.35$), a second weak recirculation region develops, initiated by the large velocity difference between the aerosol and the inner sheath flow; this is accompanied by a strengthening of the outer vortex. This structure, of a weak inner vortex accompanying a stronger outer vortex, mimics the same structure that was found (Figure S3) for the case in the absence of sheath flows. The relative strengths of the two vortices are given by the maximum values of the stream function (Table S7).

The critical aerosol flows for the onset of these recirculations were determined to be: (i) outer vortex formation at $Q_{aero} \sim 13.2$ L/min ($Q_{aero}/Q_{sh} \sim 2.93$, $v_{aero}/v_{sh} \sim 52$); (ii) inner vortex formation at $Q_{aero} \sim 15.9$ L/min ($Q_{aero}/Q_{sh} \sim 3.54$, $v_{aero}/v_{sh} \sim 50$)–these critical aerosol flows are confirmed by the full three-dimensional simulation (Table S8). Additional simulations (not reported here) confirm that these vortices may be suppressed by further increasing the sheath flows.

3.3. Pressure Variation

Figure 7 displays the pressure along the length of the FCS (at a distance $\Delta r^* = 0.042$ from the outer cylinder) for the four simulations studied (at the exit, this corresponds to a radius midway between the inner and outer cylinders). The inviscid contribution to the pressure for Case 1 is estimated (applying Bernoulli's equation along a streamline close to the converging cylinder) to be ~62% of the total pressure. For all of the simulated cases, the pressure (along the line plotted) is effectively constant along the first 80% of the FCS length, with almost 90% of the pressure drop occurring over the last 20% of the FCS length. The pressure is insensitive to the detailed structure of the upstream combination of the aerosol and sheath flows. The pressure shows no obvious signature of the recirculation regions (Cases 3 and 4). The pressure is radially quite constant (not shown here), with maximal variation of ~8% (5%) at $x^* \sim 4.2$ for Case 1 (Case 4); near the inlets, the radial variation of the pressure is also small (~0.2%).

3.4. Axial Velocity Contours and Comparison with Previous Work

The flow rates for which Deye et al. (1999) performed their calculation correspond to our Case 1. The pattern of the

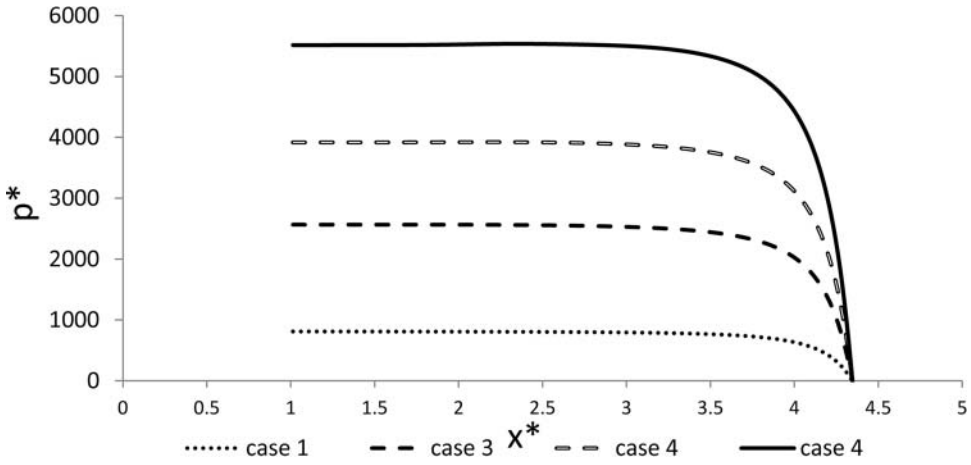

FIG. 7. Axial pressure variation inside FCS along a line parallel to outer cylinder and located at $r^* = 0.25$ at exit.

streamlines for Case 1 (Figure 6a) is similar to that of Deye et al. (1999); in particular, Deye et al. (1999) did not detect any vortex formation. The focusing, by the sheath flows, of the aerosol streamlines, as they exit from the nozzle, is common to both works. However, our axial velocity contours (Figure 8a) differ from those of Deye et al. (1999) near the inlet. Their contours indicate a higher velocity near the outer cylinder upstream. However, since the outer sheath inlet area is larger than the inner sheath inlet area, the outer sheath inlet velocity must be smaller than the inner sheath velocity. We believe the contours of Deye et al. (1999) are in error near the inlet. The general structure of the axial velocity contours (Case 1) is a ramp, increasing from the inlet nozzle to the flow combination exit, and falling off as either cylindrical wall is approached. With the increase in aerosol velocity (Figure 8b for Case 4), the recirculation regions introduce axial velocity contour wells, radially on either side of the overall ramp, and these wells tend to pinch the ramp upstream.

3.5. Discussion of the Recirculation Regime

It is instructive to consider the aerodynamics of the FCS confined laminar annular jet in two ways: (i) with a time-dependent description and (ii) within a steady-state description.

When a circular jet discharges into an unconfined quiescent fluid, the boundary layer on the jet nozzle forms a free shear layer, originating at the nozzle lip and extending downstream (Reynolds et al. 2003). This shear layer is subject to a Kelvin–Helmholtz instability (Schlichting 1933; Ho and Huerre 1984). Axisymmetric ring vortices form in the jet shear layers. These vortices are advected downstream, interact, detach, become unstable, and break down, giving rise to downstream turbulence in the far field.

When the jet is confined (as by the outer and inner cylinders of the FCS), the time-dependent behavior may be stabilized due to competition between vorticity generation at, and its diffusion away from, the jet boundary layers. If the out-diffusion dominates (Figure S2a: $\mathrm{Re}_{\mathrm{aerosol}} \sim 13$, $\mathrm{Re}_{\mathrm{out}} \sim 25$, $\mathrm{Re}_{\mathrm{in}} \sim 50$), vortex rings do not form. If the out-diffusion balances the vorticity generation (Figure S2b: $\mathrm{Re}_{\mathrm{aerosol}} \sim 117$, $\mathrm{Re}_{\mathrm{out}} \sim 25$, $\mathrm{Re}_{\mathrm{in}} \sim 50$), a steady-state recirculation develops downstream of the nozzle; in the FCS, the radial asymmetry of the nozzle introduces asymmetry in the generation of the inner and outer vortices. Presumably, at still higher Re (which we did not investigate), the flow will become time-dependent, unstable, and, ultimately, turbulent.

The effects of confinement may also be understood within a steady-state description (Landfried et al. 2012). When a steady-state jet discharges into an unconfined quiescent fluid, the external fluid is entrained, and the jet spreads (Pai 1954). Confinement of the external fluid restricts this entrainment. If the jet is confined purely by a lateral cylindrical wall (a "ventilated jet"), fluid upstream from the jet nozzle may still be entrained, and the jet spreads to the confining wall. If, however, there is also a back wall, obstructing the axial flow exterior to the jet nozzle, recirculation of the "dead fluid" is induced as the jet spreads. If the back wall is sufficiently far upstream from the nozzle, the recirculation occurs exterior to and upstream of the nozzle, and the jet spreads, essentially as

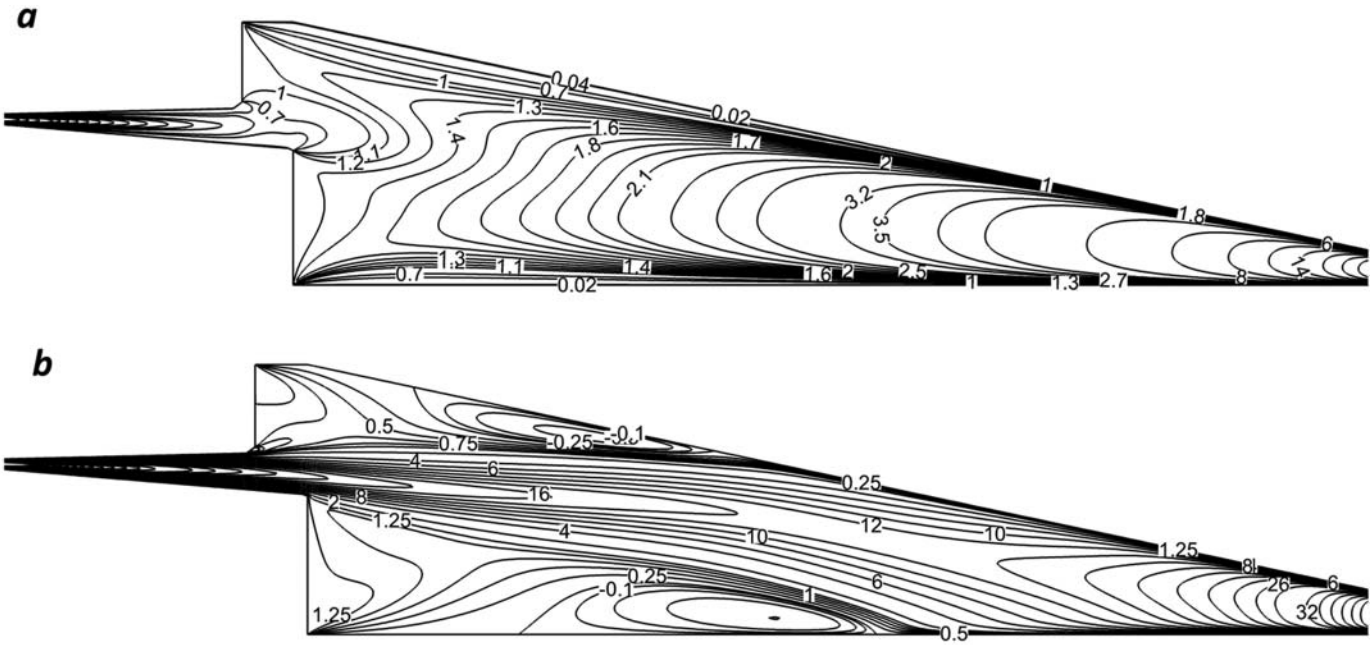

FIG. 8. Non-dimensional axial velocity contours for (a) Case 1 and (b) Case 4.

it would were there no back wall present (Landfried et al. 2012). If, however, the back wall is flush with the nozzle, then the recirculation is forced downstream and interferes with the spreading of the jet–this is precisely the geometry of the Baron FCS. The recirculation transition may be understood as a cross-over from the low aerosol flow regime (Figure S2a), where there is sufficient exterior sheath flow to permit entrainment, to the high aerosol flow regime (Figura S2b), where there is insufficient exterior sheath flow for the entrainment, and recirculation occurs downstream of the nozzle.

Of importance for a particular aerosol instrument is the prevention/control of this recirculation through various instrumental innovations. The tapered FCS design delays the appearance of both the outer recirculation to $\mathrm{Re}_{\mathrm{aerosol}} \sim 171$ ($\Delta\mathrm{Re} = \mathrm{Re}_{\mathrm{aerosol}} - \mathrm{Re}_{\mathrm{out}} \sim 146$) and the inner recirculation to $\mathrm{Re}_{\mathrm{aerosol}} \sim 204$ ($\Delta\mathrm{Re} = \mathrm{Re}_{\mathrm{aerosol}} - \mathrm{Re}_{\mathrm{in}} \sim 154$). The CFD simulation demonstrates how this conical convergence in a real instrument stabilizes the flow against formation of outer and inner vortices ($Q_{\mathrm{aero}}/Q_{\mathrm{sheath}} \sim 8.1, 9$ goes to 13.2, 15.8).

The usefulness of the tapered geometry to stabilize flows, where aerosol and sheaths are introduced, has long been appreciated by aerosol instrument designers; however, to our knowledge, elucidation of the alternative flow patterns that actually develop within the mixing region, and their quantitative suppression by the tapered geometry, has not been explicitly pointed out to the aerosol community.

4. CONCLUSION

With the current flow rates used by NIOSH, our CFD study indicates that the flow inside the FCS is free from any separation or vortex formation (Case 1). One of the key findings of this paper is the onset of weak recirculation when the ratio of aerosol inlet velocity to the sheath inlet velocity exceeds 50. This recirculation region becomes more prominent as the ratio of the velocities increases. Owing to the nozzle shape, the aerosol tends to spread out as it enters the FCS. However, sheath flows, in conjunction with the conically converging outer wall, are effective in preventing aerosol deposition on the FCS walls. The aerosol remains in the middle region between the two cylinders at the exit in the four cases studied. The aerosol is well confined to the center of the exit annulus; as the aerosol flow rate is increased, the aerosol spreads out and progressively occupies a larger fraction of the exit annulus. This finding is also supported by the shear stress profiles at the exit. Near the exit, the shear stress vanishes around the middle region, precisely where the aerosol fibers are expected to be concentrated. In all the cases studied, despite the detailed flow variations within the FCS itself, the instrument design is sufficiently robust so that the aerosol velocity evolves to the desired parabolic flow profile, with the concomitant desired sigmoidal shear stress profile, upon exiting the FCS and entering the flow classification section (the working portion of the instrument).

NIOSH has a long-standing program to test whether fiber length is a salient variable in asbestos toxicity. The Baron fiber classifier has demonstrated utility as an analytical instrument to separate fibers by length so as to characterize fiber samples. However, in order to be useful as a sample-prep instrument (for toxicology studies), the throughput of the instrument must be increased. Given that current aerosolization techniques can only achieve an aerosol concentration of $n \sim 6 \times 10^4$ fibers/cm^3, one way to increase the instrument throughput would be to increase the aerosol flow rate through the instrument. This motivated the present CFD study–a use of CFD to probe inherent limiting operational parameters of the instrument.

The results of this CFD study lend confidence that the aerosol flow rate may be increased by an order of magnitude before the new flow pattern is established. This upper limit on the aerosol flow rate essentially sets a limit on the instrument throughput. Of course, the actual performance of the instrument will probably degrade as the aerosol flow rate is increased (q.v. the brief discussion of DMA resolution)–we have yet to assess whether this resolution degradation compromises the usefulness of the instrument at these flow rates. To increase, the flow rates will involve significant instrument modifications. However, the encouraging results of this CFD study support such an approach to increasing the instrument throughput.

ACKNOWLEDGMENTS

We thank G. J. Deye, J. Bennett, and P. Kulkarni for helpful discussions. We thank our referees for their thoughtful comments.

FUNDING

This work was supported, in part, under the NIOSH NORA program.

DISCLAIMER

The findings and conclusion in this report are those of the authors and do not necessarily represent the views of the National Institute of Occupational Safety and Health. Mention of product or company name does not constitute endorsement by the Centers for Disease Control and Prevention. None of the authors has a financial relationship with a commercial entity that has an interest in the subject of this manuscript.

SUPPLEMENTARY MATERIAL

Supplemental data for this article can be accessed on the publisher's website.

REFERENCES

Baron, P., Deye, G. J., Aizenburg, V., and Castranova, V. (2002). Generation of Size-Selected Fibers for a Nose-Only Inhalation Toxicity Study. *Ann. Occ. Hyg.,* 46(Suppl. 1):186–190 (in *Inhaled Particles IX*, T. Ogden, K. Donaldson, and N. Cherry, eds., Oxford University Press, Oxford).

Baron, P. A. (1993). Measurement of Asbestos and Other Fibers, in *Aerosol Measurement: Principles, Techniques and Applications*, K. Willeke and P. A. Baron, eds., Van Nostrand Reinhold, New York, NY, pp. 560–590.

Baron, P. A., Deye, G. J., and Fernback, J. (1994). Length Separation of Fibers. *Aerosol Sci. Technol.*, 21(2):179–192.

Baron, P. A., Sorensen, C. M., and Brockmann, J. M. (2001). Nonspherical Particles: Shape Factor, Fractals and Fibers, in *Aerosol Measurement: Principles, Techniques and Applications*, 2nd ed., P. A. Baron and K. Willeke, eds., J. Wiley & Sons, Hoboken, NJ, pp. 705–749.

Blake, T., Castranova, V., Baron, P., Schwegler-Berry, D., Deye, G. J., Li, C., and Jones, W. (1998). Effect of Fiber Length on Glass Microfiber Cytotoxicity. *J. Toxicol. Environ. Health A*, 54:243–259.

Castranova, V., Jones, W., Blake, T., Ye, J., She, X., Deye, G., and Baron, P. (2000). Critical Role of Fiber Length in the Bioactivity and Cytotoxicity of Glass Fibers. *Toxicol.*, 54(Suppl. 1):319 (paper 1495).

Castranova, V., Pailles, W., Judy, D., Blake, T., Schwegler-Berry, D., and Jones, W. (1996). In vitro Effects of Large and Small Glass Fibers on Rat Alveolar Macrophages. *J. Toxicol. Environ. Health*, 49: 357–369.

Castranova, V., Zeidler, P. C., Calhoun, W. T., Ameredes, B. T., Clark, M. P., Deye, G., Baron, P., and Blake, T. (2003). Cytotoxicity of Size-Selected Manville Code 100 (JM-100) Glass Fibers on Human Alveolar Macrophages. *Toxicologist*, 72(Suppl. 1):45 (paper 218).

Celik, I. B., Ghia, U., Roache, P. J., Freitas, C. J., Coleman, H., and Raad, P. E. (2008). Procedure for Estimation and Reporting of Uncertainty due to Discretization in CFD Applications. *J. Fluids Eng.*, 130(7):078001–078004.

Deye, G. J., Gao, P., Baron, P. A., and Fernback, J. (1999). Performance Evaluation of a Fiber Length Classifier. *Aerosol Sci. Technol.*, 30:420–437.

Dou, H. S., Khoo, B. C., and Tsai, H. M. (2010). Determining the Critical Condition for Turbulent Transition in a Fully-Developed Annulus Flow. *J. Petroleum Sci. Eng.*, 73:41–47.

Flagan, R. C. (1998). History of Electrical Aerosol Measurements. *Aerosol Sci. Technol.*, 28:301–380.

Flagan, R. C. (1999). On Differential Mobility Analyzer Resolution. *Aerosol Sci. Technol.*, 30:556–570.

Flagan, R. C. (2001). Electrical Techniques, in *Aerosol Measurement: Principles, Techniques and Applications*, 2nd ed., Baron, P. A. and K. Willeke, eds., J. Wiley & Sons, Hoboken, NJ, pp. 537–568.

Han, R. J., Moss, O. R., and Wong, B. A. (1994). Airborne Fiber Separation by Electrophoresis and Dielectrophoresis: Theory and Design Considerations. *Aerosol Sci. Technol.*, 21:241–258.

Hanks, R. W., and Bonner W. F. (1971). Transitional Flow Phenomena in Concentric Annuli. *Indust. Eng. Chem. Fundam.*, 10(1):105–113.

Hart, G. A., Kathman, L. M., and Hesterberg, T. W. (1994). In vitro Cytotoxicity of Asbestos and Man-Made Vitreous Fibers: Roles of Fiber Length, Diameter and Composition. *Carcinogenesis*, 15(5):971–977.

Ho, C. M., and Huerre, P. (1984). Perturbed Free Shear Layers. *Ann. Rev. Fluid Mech.*, 16:365–424.

Knutson, E. O., and Whitby, K. T. (1975). Aerosol Classification by Electric Mobility: Apparatus, Theory and Applications. *J. Aerosol Sci.*, 6:443–451.

Landfried, D. T., Jana, A., and Kimber, M. L. (2012). Characterization of the Behavior of Confined Laminar Round Jets. *ASME Proceedings–FEDSM2012–72257 (Proceedings IB: 1037–1046)*.

Lilienfeld, P. (1985). Rotational Electrodynamics of Airborne Fibers. *J. Aerosol Sci.*, 16(4):315–322.

Lipowicz, P. J., and Yeh, H. C. (1989). Fiber Dielectrophoresis. *Aerosol Sci. Technol.*, 11(3):206–212.

Lippmann, M. (1990). Effects of Fiber Characteristics on Lung Deposition, Retention, and Disease. *Environ. Health Perspect.*, 88:311–317.

Loomis, D., Dement, J., Richardson, D., and Wolf, S. (2010). Asbestos Fibre Dimensions and Lung Cancer Mortality Among Workers Exposed to Chrysotile. *Occup. Environ. Med.*, 67:580–584.

Middendorf, P., Zumwalde, R., Castellan, R., Harper, M., Wallace, W., Stayner, L., Castranova, V., Hearl, F., and Sullivan, P. (2011). *Asbestos Fibers and Other Elongated Mineral Particles: State of the Science and Roadmap for Research*. NIOSH Current Intelligence Bulletin 62 (DHHS publication number 2011-159). U.S. Department of Health and Human Services, Cincinnati, OH.

Pai, S. I. (1954). *Fluid Dynamics of Jets*. Van Nostrand, New York.

Patankar, S. V. (1980). *Numerical Heat Transfer and Fluid Flow*. Hemisphere Publishing Corp., Washington, DC.

Reynolds, W. C., Parekh, D. E., Juvet, P. J. D., and Lee, M. J. D. (2003). Bifurcating and Blooming Jets. *Ann. Rev. Fluid Mech.*, 35:295–315.

Schlichting, H. (1933). Laminare Strahlausbreitung. *Z. Angew. Math. Mech.*, 13:260–263.

Stayner, L., Kuempel, E., Gilbert, S., Hein, M., and Dement, J. (2008). An Epidemiological Study of the Role of Chrysotile Asbestos Fibre Dimensions in Determining Respiratory Disease Risk in Exposed Workers. *Occup. Environ. Med.*, 65:613–619.

Turkevich, L. A., and Deye, G. (2011). Advances in Techniques for Mineral Fiber Classification, in *NORA Symposium 2011. Achieving Impact Through Research and Partnerships*, Centers for Disease Control and Prevention, US Department of Health and Human Services, Cincinnati, OH.

Wang, Z., Hopke, P., Baron, P. A., Ahmadi, G., Cheng, Y.-S., Deye, G., and Su, W.-C. (2005). Fiber Classification and the Influence of Average Air Humidity. *Aerosol Sci. Technol.*, 39:1056–1063.

Ye, J., Shi, X., Jones, W., Rojanasakul, Y., Cheng, N., Schwegler-Berry, D., Baron, P., Deye, G. J., Li, C., and Castranova, V. (1999). Critical Role of Glass Fiber Length in TNF-α Production and Transcription Factor Activation in Macrophages. *Am. J. Physiol.: Lung Physiol.*, 276(3): 426–434.

Zeidler, P. C., Ye, J., Jones, W., Baron, P., Martinez, A., Robinson, V. A., Landsittel, D. P., and Castranova, V. (2001) Use of Size-Selected Fibers to Evaluate the Contribution of Length vs. Chemistry in Fiber Cytotoxicity. *Tox. Sci.*, 60(Suppl. 1):198 (paper 942).

Zeidler-Erdelyi, P. C., Calhoun, W. J., Ameredes, B. T., Clark, M. P., Deye, G., Baron, P., Jones, W., Blake, T., and Castranova, V. (2006). In vitro Cytotoxicity of Manville Code 100 Glass Fibers: Effect of Fiber Length on Human Alveolar Macrophages. *Part. Fibre Tox.*, 3:5–12.